

# Geophysical Research Letters<sup>®</sup>



## RESEARCH LETTER

10.1029/2024GL111835

### Key Points:

- A new seismic azimuthally anisotropic model of the Juan de Fuca-Gorda plate system is constructed based on surface waves
- Paleo-spreading explains most of azimuthal anisotropy within the shallow oceanic lithosphere
- Azimuthal anisotropy in the asthenosphere reflects plate shear as inferred from the NUVEL1A plate motion model

### Supporting Information:

Supporting Information may be found in the online version of this article.

### Correspondence to:

C. Liu,  
[chuanming.liu@jsg.utexas.edu](mailto:chuanming.liu@jsg.utexas.edu)

### Citation:

Liu, C., Becker, T., Wu, M., Han, S., & Ritzwoller, M. H. (2024). Seismic azimuthal anisotropy within the Juan de Fuca - Gorda plate system. *Geophysical Research Letters*, 51, e2024GL111835. <https://doi.org/10.1029/2024GL111835>

Received 8 AUG 2024

Accepted 22 OCT 2024



### Author Contributions:

**Conceptualization:** Chuanming Liu  
**Data curation:** Mengyu Wu  
**Formal analysis:** Chuanming Liu  
**Funding acquisition:** Chuanming Liu, Michael H. Ritzwoller  
**Investigation:** Chuanming Liu  
**Methodology:** Chuanming Liu  
**Software:** Chuanming Liu  
**Supervision:** Thorsten Becker, Michael H. Ritzwoller  
**Visualization:** Chuanming Liu  
**Writing – original draft:** Chuanming Liu  
**Writing – review & editing:** Chuanming Liu, Thorsten Becker, Mengyu Wu, Shuoshuo Han, Michael H. Ritzwoller

© 2024. The Author(s).

This is an open access article under the terms of the [Creative Commons Attribution-NonCommercial-NoDerivs](https://creativecommons.org/licenses/by/4.0/) License, which permits use and distribution in any medium, provided the original work is properly cited, the use is non-commercial and no modifications or adaptations are made.

## Seismic Azimuthal Anisotropy Within the Juan de Fuca - Gorda Plate System

Chuanming Liu<sup>1,2</sup> , Thorsten Becker<sup>1,2,3</sup> , Mengyu Wu<sup>4</sup> , Shuoshuo Han<sup>1</sup> , and Michael H. Ritzwoller<sup>4</sup>

<sup>1</sup>Institute for Geophysics, Jackson School of Geosciences, The University of Texas at Austin, Austin, TX, USA,

<sup>2</sup>Department of Earth and Planetary Sciences, Jackson School of Geosciences, The University of Texas at Austin, Austin, TX, USA, <sup>3</sup>Oden Institute for Computational Engineering & Sciences, The University of Texas at Austin, Austin, TX, USA,

<sup>4</sup>Department of Physics, University of Colorado Boulder, Boulder, CO, USA

**Abstract** We estimate seismic azimuthal anisotropy for the Juan de Fuca - Gorda plates from inversion of a new 10–80 s period Rayleigh wave dataset, resulting in a two-layer model to 80 km depth. In the lithosphere, most anisotropy patterns reflect the kinematics of plate formation, as approximated from seafloor-age-based paleo-spreading, except for regions close to propagator wakes and near plate boundaries. In the asthenosphere, the fast propagation orientations align with convective shear as inferred from the NUVEL1A plate motion model, which is indicative of a ~3 Myr average, rather than with the more recent, ~0.8 Myr, motions inferred from MORVEL. Regional anisotropy of this young plate system thus records convection like older plates such as the Pacific. On smaller scales, anisotropy imaging provides insights into dynamics of plate generation and can further elucidate plate reorganizations and changes in boundary loading.

**Plain Language Summary** The speed of seismic waves can depend on the direction the wave travels, a phenomenon known as seismic azimuthal anisotropy. Below the Earth's crust, this property is linked to the alignment of olivine fabrics under deformation in the oceanic lithosphere and asthenosphere, allowing us to infer spreading histories and mantle flow. Here, we construct a new 3-D model of seismic azimuthal anisotropy for the Juan de Fuca - Gorda plate system. The fast propagation orientation of azimuthal anisotropy in most of the lithosphere records paleo-spreading, and the asthenosphere mantle flow as inferred from a longer-term plate motion model, although not the most recent convergence directions. These findings indicate that this young oceanic plate system has similar azimuthal anisotropy properties to older plates and shallow anisotropy can be used to understand the evolution of the plate system.

## 1. Introduction

Seismic anisotropy is one of the most important observables for decoding the tectonic history and dynamics of oceanic plate systems (e.g., Long & Becker, 2010; Tanimoto & Anderson, 1984). Below the crust, in the olivine-dominated oceanic lithosphere and asthenosphere, the connection between seismic anisotropy and convective dynamics or tectonic processes is simpler than in continental plates (e.g., Becker & Lebedev, 2021; Conrad & Lithgow-Bertelloni, 2007; Liu & Ritzwoller, 2024), due to the relative compositional simplicity and shorter deformation history.

The primary cause of seismic anisotropy in the oceanic lithosphere and upper mantle is the formation of crystallographic-preferred orientation (CPO) of olivine fabrics. CPO results from past and current convective deformation, predominantly under dislocation creep, encoding information about finite strain and CPO reworking (Karato et al., 2008; Nicolas & Christensen, 1987). In the oceanic lithosphere, seismic anisotropy is thought to be mainly frozen-in, that is, CPO that formed at the spreading center, or mid-ocean ridge (MOR), recording the relative plate motion, then not further modified due to cooling and reduced strain rates, leaving a record of paleo-spreading (e.g., Becker et al., 2014; Francis, 1969; Nishimura & Forsyth, 1989; D. B. Smith et al., 2004). In the underlying oceanic asthenosphere, seismic anisotropy mainly reflects CPO formation and reworking under the influence of convective mantle flow, indicating shear in mantle flow through the fast orientations of seismic anisotropy (e.g., Becker et al., 2014; Debayle & Ricard, 2013; Tanimoto & Anderson, 1984).

The Juan de Fuca - Gorda (JdFG) plate system is an interesting region to investigate the tectonic processes of oceanic plate generation and the geodynamics of the asthenosphere using seismic anisotropy, due to its young age,

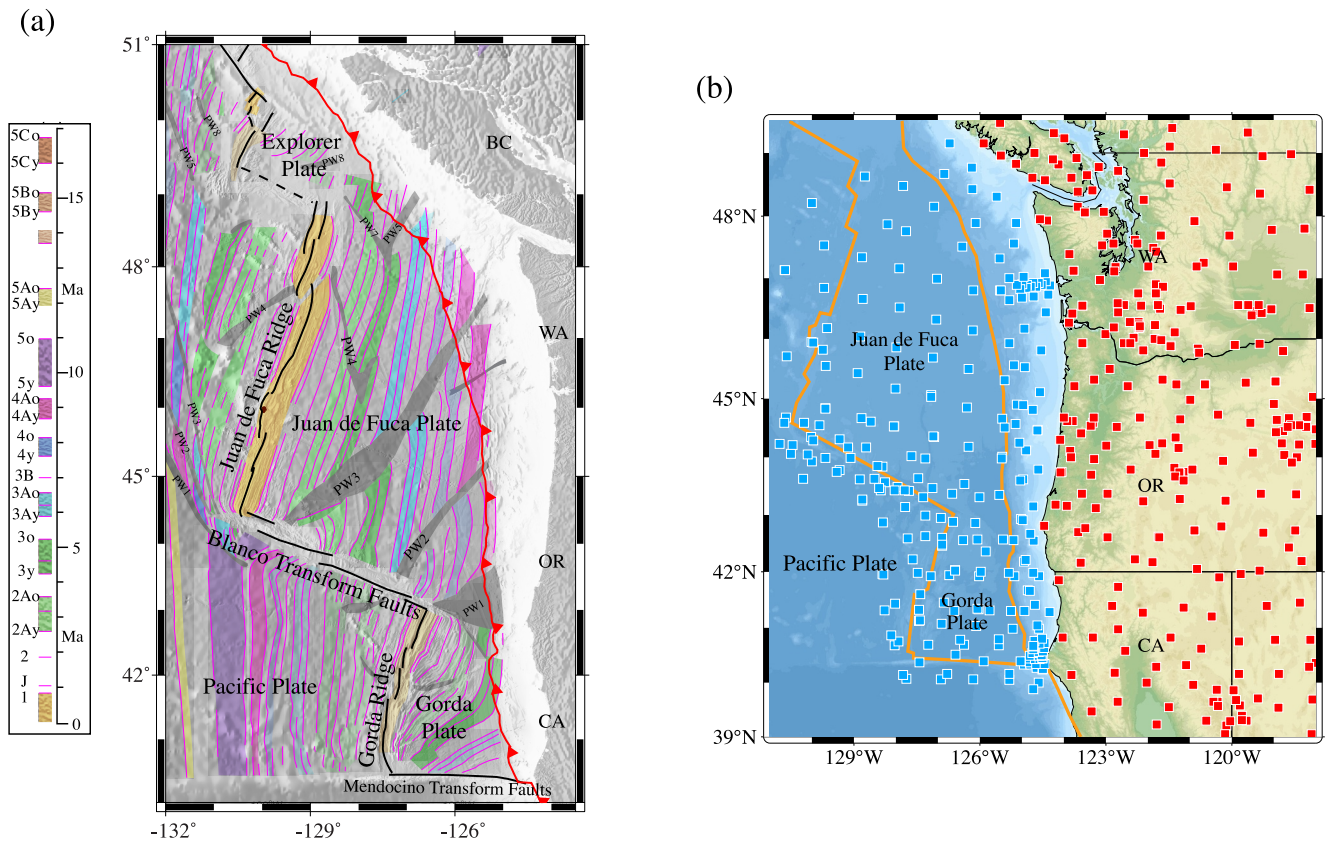


**Figure 1.** (a) Tectonic setting of the Juan de Fuca and Gorda plate system. The colored bands represent magnetic anomalies, pink lines indicate magnetic isochrons and gray shading outlines propagator wakes (Nedimović et al., 2009; Wilson, 1988, 1993). The figure is modified from Nedimović et al. (2009). BC = British Columbia; WA = Washington; OR = Oregon; CA = California; PW = propagator wake. (b) Seismic stations: red squares mark onshore and blue squares mark OBS instruments.

and its proximity to the continent which makes it more readily observable (Figure 1a). The JdFG system is the northernmost remnant of the Farallon plate where the full spreading rate is currently 56 mm/yr for the Juan de Fuca (JdF) and northern Gorda Ridge (Wilson, 1993), while it decreases to approximately 10 mm/yr for the southern Gorda Ridge (Riddihough, 1984). Compared to the Juan de Fuca plate, the Gorda plate experiences significant internal deformation and reorganization with a significant amount of intraplate seismicity (Chaytor et al., 2004; Wilson, 1988).

Benefitting from the deployment of seismometers of the Cascadia Initiative experiment (CI; Toomey et al., 2014) across the Juan de Fuca-Gorda plate and Cascadia, the seismic anisotropy structure of the Juan de Fuca-Gorda plate has been investigated using various seismic approaches. Bodmer et al. (2015) and Martin-Short et al. (2015) used *SKS* splitting to investigate the path-integrated anisotropy of the upper mantle. By employing *P<sub>n</sub>* tomography, VanderBeek and Toomey (2017, 2019) constructed P-wave anisotropy models near the Moho in the Gorda plate, and a plate-average-only model in the JdF plate due to limited azimuthal coverage. Eilon and Forsyth (2020) resolved a depth-dependent but also plate-averaged anisotropy based on the joint inversion of teleseismic Rayleigh waves (20–125 s) and *SKS* splits. Ren et al. (2024) used teleseismic Rayleigh waves (25–100 s) to infer mainly mantle azimuthal anisotropy variations. A 3-D, depth-dependent seismic anisotropy model involving shallow depths and spanning the entire JdFG system remains to be established. Such a model is important to help resolve questions about the cause of seismic anisotropy at different depths in a young and moderate-speed spreading oceanic plate, and to explore how shallow anisotropy patterns may complement magnetic anomalies to help decipher the details of plate generation.

Here, we construct such a 3-D azimuthal anisotropy model of the crust and uppermost mantle of the Juan de Fuca-Gorda plate system. We use a new Rayleigh wave dispersion database based on two- and three-station ambient noise interferometry and earthquake data (Zhang et al., 2021a), as well as a new *V<sub>S</sub>* reference model (Wu

et al., 2023; Wu & Ritzwoller, 2023). The application of the three-station ambient noise method improves azimuthal and ray-path coverage at short periods (10–40 s) by linking asynchronous station pairs. This is important for the asynchronously deployed CI OBS arrays (from 2011 to 2013 mostly in the Juan de Fuca plate; 2012–2014 in the Gorda plate). Based on our new azimuthal anisotropy model, we investigate the relationship between the fast orientation of seismic anisotropy, the paleo-spreading direction, and mantle shear as approximated from different absolute plate motion (APM) models. Results have implications for the origin of seismic anisotropy in the oceanic lithosphere and asthenosphere in general.

## 2. Data and Inversion

### 2.1. Data

We apply Rayleigh wave phase speed dispersion measurements (10–80 s) from the dataset of Zhang et al. (2021a). These measurements were obtained from two- and three-station ambient noise interferometry and teleseismic events recorded at 252 OBS and 360 onshore seismic stations. The linked asynchronous CI OBS stations by using the three-station method in the JdF and the Gorda plate improved azimuthal coverage for the subsequent seismic azimuthal anisotropy inversion, similar to work in the Aleutian subduction zone (Liu et al., 2022).

For a given frequency, the local Rayleigh wave phase speed in a weakly anisotropic medium for a wave propagating at azimuth  $\psi$  can be represented approximately by  $2\psi$  anisotropy (e.g., M. L. Smith & Dahlen, 1973) and possible apparent  $1\psi$  anisotropy (e.g., Lin & Ritzwoller, 2011):

$$c(\psi) = c_{iso} + \delta c_{AA}(\psi) \approx c_{iso} \left( 1 + \frac{A_1}{2} \cos(\psi - \psi_1) + \frac{A_2}{2} \cos(2(\psi - \psi_2)) \right), \quad (1)$$

where  $c_{iso}$  is the isotropic phase speed,  $\delta c_{AA}$  is the azimuthal anisotropy perturbation,  $\psi_1$  and  $\psi_2$  are the fast axis orientations for the  $1\psi$  and  $2\psi$  components of anisotropy, and  $A_1$  and  $A_2$  are the peak-to-peak relative amplitudes for  $1\psi$  and  $2\psi$  anisotropy, respectively. Orientation angles,  $\psi$ , are taken positive clockwise from North. The  $1\psi$  anisotropy is typically strong at long periods (>50 s) and is not caused by intrinsic anisotropy, but is an isotropic phenomenon that may be caused by several effects, including Rayleigh wave back-scattering (Lin & Ritzwoller, 2011). For the dataset we used, Zhang et al. (2021a) observed relatively strong  $1\psi$  anisotropy at long periods (>50 s), and its influence is reduced by considering finite frequency effects using Helmholtz tomography at long periods. The uncertainty estimates for  $c_{iso}$  and  $\delta c_{AA}$  are obtained by fitting Equation 1 to binned observations from both ambient noise and earthquake measurements. The uncertainties of the isotropic and anisotropic measurements are upscaled to account for the systematic errors. Details on the dataset construction and uncertainty analysis are described by Zhang et al. (2021a) and Wu et al. (2023). In our study, we directly use the Rayleigh wave phase velocity  $2\psi$  azimuthal anisotropy (fast axis,  $\psi_2$ , and amplitude,  $A_2$ ) and corresponding uncertainties.

### 2.2. Inversion Method

We use a two-step inversion procedure to resolve depth-dependent shear wave azimuthal anisotropy, following Liu, Sheehan, and Ritzwoller (2024). First, we assimilate a 3-D isotropic  $V_S$  model from the set of local vertical 1-D isotropic  $V_S$  profiles from a  $0.4^\circ$  by  $0.4^\circ$  grid across the study region by Wu et al. (2023). Each 1-D isotropic  $V_S$  model is inverted from surface wave dispersion data using a thermo-seismic hybrid parameterization, where the lithosphere is parameterized with apparent thermal age (cf. Ritzwoller et al., 2004). Details of the isotropic inversion and the  $V_S$  model are discussed by Wu et al. (2023).

In the second step, we invert Rayleigh wave phase velocity azimuth anisotropy at periods from 10 to 80 s for the depth-dependent shear wave azimuth anisotropy at each grid point and then combine the individual models into a model of 3-D azimuthal anisotropy. The Rayleigh wave phase velocity  $2\psi$  azimuthal anisotropy perturbation is linked to a transversely isotropic medium with a horizontal symmetry axis (a so-called HTI medium) by

$$\delta c_{AA_{2\psi}}(T, \psi) = \int \left\{ \left( G_c \frac{\partial c_R}{\partial L} + B_c \frac{\partial c_R}{\partial A} + H_c \frac{\partial c_R}{\partial F} \right) \cos 2\psi + \left( G_s \frac{\partial c_R}{\partial L} + B_s \frac{\partial c_R}{\partial A} + H_s \frac{\partial c_R}{\partial F} \right) \sin 2\psi \right\} dz \quad (2)$$

(Montagner & Nataf, 1986), where  $\delta c_{AA}$  is defined by Equation 1,  $T$  is the period, and the anisotropic shear moduli  $G_{c,s}$ ,  $B_{c,s}$ , and  $H_{c,s}$  represent the  $2\psi$  azimuthal variations for three ( $L$ ,  $A$ , and  $F$ ) of the five Love moduli

( $A = \rho V_{PH}^2$ ,  $C = \rho V_{PV}^2$ ,  $L = \rho V_{SV}^2$ ,  $N = \rho V_{PH}^2$ , and  $F$ ), and  $\frac{\partial c_R}{\partial L}$ ,  $\frac{\partial c_R}{\partial A}$ , and  $\frac{\partial c_R}{\partial F}$  are the sensitivity kernels for  $L$ ,  $A$ , and  $F$ , respectively. We ignore the term  $H_{c,s}$  due to its small effect on Rayleigh waves (e.g., Montagner & Nataf, 1986). We also impose the *a priori* relationship,  $\frac{B_{c,s}}{A} = \frac{G_{c,s}}{L}$ , following Lin et al. (2011), Feng et al. (2020), and Liu et al. (2019, 2024). Equation 2 can then be written approximately as

$$\delta c_{AA_{2\psi}}(T, \psi) \approx \int_0^\infty \left\{ \left( \frac{\partial c_R}{\partial L} + \frac{A}{L} \frac{\partial c_R}{\partial A} \right) G_c \cos 2\psi + \left( \frac{\partial c_R}{\partial L} + \frac{A}{L} \frac{\partial c_R}{\partial A} \right) G_s \sin 2\psi \right\} dz. \quad (3)$$

In Equation 2, we only estimate the anisotropic shear moduli  $G_{c,s}$  using the Bayesian Monte Carlo inversion method (Liu, Sheehan, & Ritzwoller, 2024). The depth-dependent fast azimuth,  $\phi_{SV}$ , and anisotropy amplitude,  $A_{SV}$ , are determined from  $G_s$  and  $G_c$  as follows:

$$\phi_{SV} = \frac{1}{2} \tan^{-1} \left( \frac{G_s}{G_c} \right), \quad (4)$$

and

$$A_{SV} = \frac{1}{2} \sqrt{\left( \frac{G_s}{L} \right)^2 + \left( \frac{G_c}{L} \right)^2}. \quad (5)$$

To first order, averaging of the  $G_s$  and  $G_c$  moduli using Equations 4 and 5 also provides a link between surface wave anisotropy and shear wave splitting (Becker et al., 2012; Montagner et al., 2000). The lateral resolution of the final azimuthal anisotropy model is primarily controlled by the smoothing applied during the tomographic step, which is approximately 130 km (Zhang et al., 2021a). The uncertainty estimation for the first-step isotropic and second-step anisotropic inversions is performed independently by Wu et al. (2023) and in the section below, respectively.

### 2.3. Model Parameterization

Our 3-D model of azimuthal anisotropy is composed of a set of vertical 1-D models at each node on a  $0.4^\circ$  by  $0.4^\circ$  grid. We parameterize the azimuthal anisotropy using three dominant depth-dependent layers: a lithospheric layer (from the bottom of the sediments to 20 km below the Moho), an asthenospheric zone (50 km thick layer beneath the lithosphere layer), and a complementary deeper asthenosphere layer extending from the bottom of the upper asthenospheric layer to 200 km depth, which is mainly constrained by longer period measurements. The water and sedimentary layers are set as isotropic. This layered structure is based on the variation of Rayleigh phase velocity fast orientation patterns at different periods (Figure S1 in Supporting Information S1) and is also motivated by the results of Eilon and Forsyth (2020). We also tested the anisotropy model with an isotropic oceanic crust. The isotropic crust setting results in relatively large anisotropy amplitudes in the lithospheric and asthenospheric layers, while still showing very similar fast orientation patterns. Details about this model are in Text S1 in Supporting Information S1.

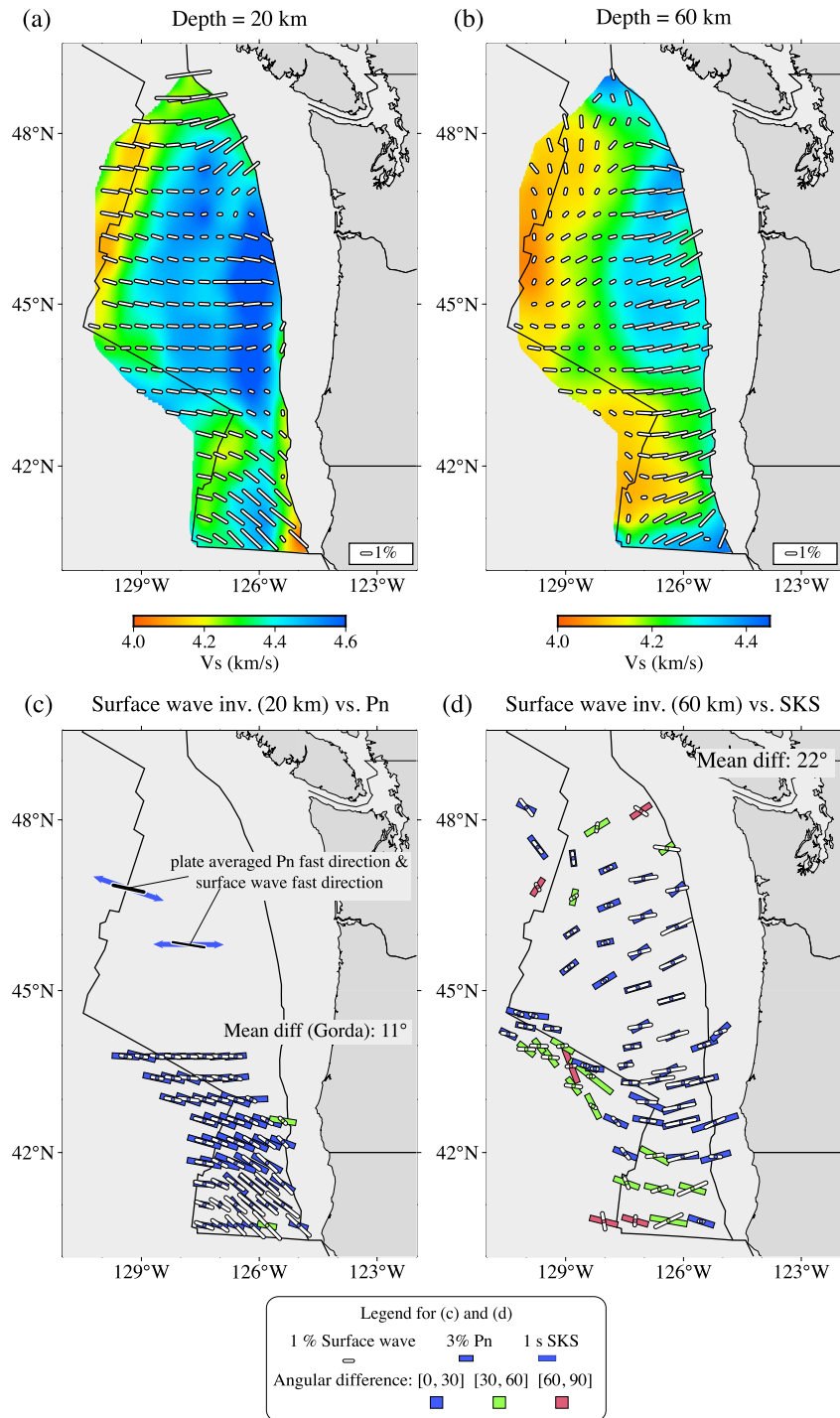
We use a Bayesian Monte Carlo method (Liu, Sheehan, & Ritzwoller, 2024) to invert Rayleigh wave phase speed azimuth anisotropy ( $\psi_2, A_2$ ) measurements for depth-dependent azimuthal anisotropy ( $\phi_{SV}, A_{SV}$ ). The depth-dependent azimuthal anisotropy parameters ( $\phi_{SV}, A_{SV}$ ) are constant in the three layers. The prior distributions for these variables are uniform in  $[0^\circ, 180^\circ]$  for  $\phi_{SV}$  and  $[0, 5\%]$  for  $A_{SV}$ . Uncertainties for azimuthal anisotropy variables ( $\phi_{SV}, A_{SV}$ ) are estimated from one standard deviation of the posterior distribution.

## 3. Results

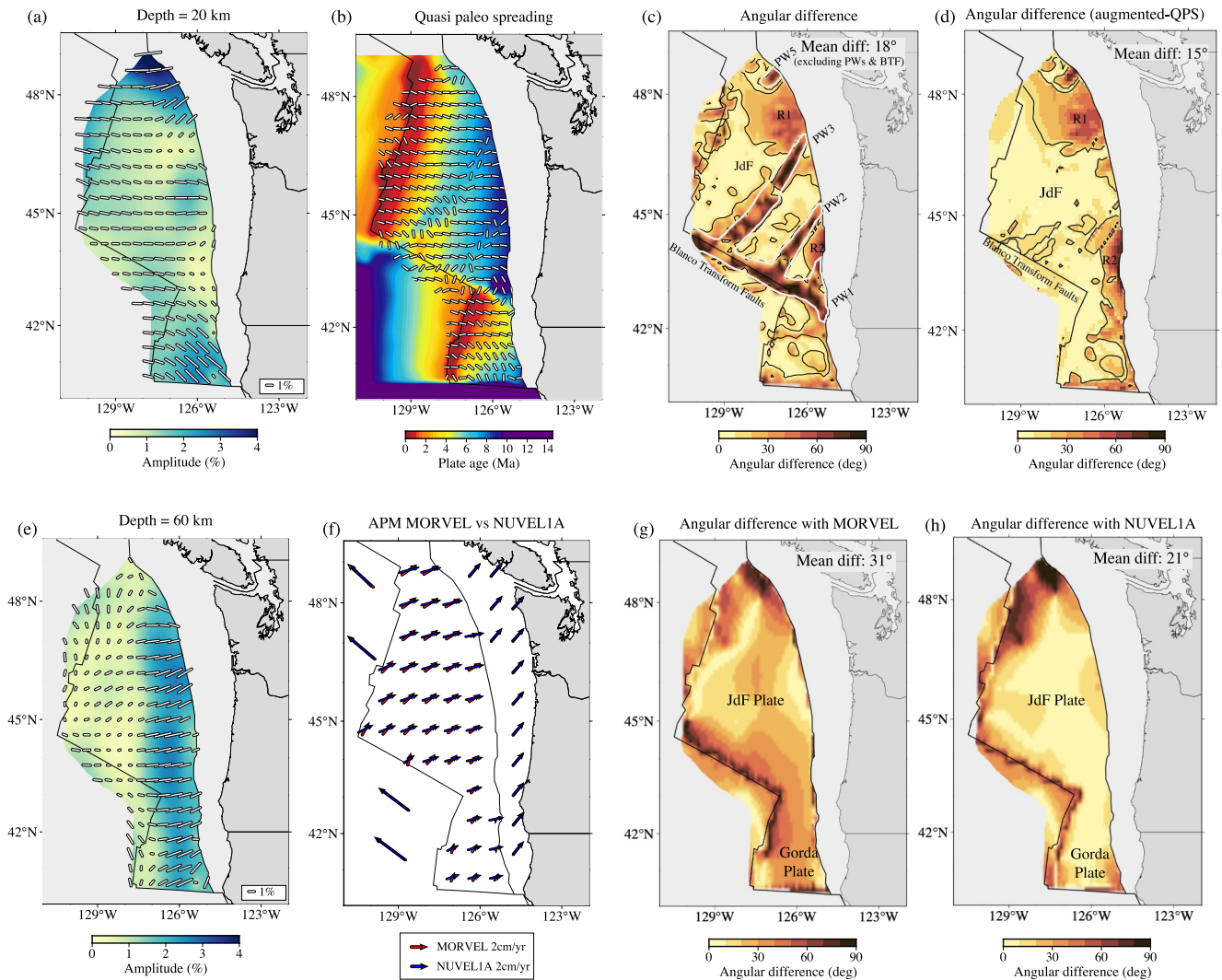
We focus our discussion on the mean and standard deviation of the posterior distribution for azimuthal anisotropy fast orientation and amplitude ( $\phi_{SV}$  and  $A_{SV}$ ) as functions of depth. An example of the posterior distributions for  $\phi_{SV}$  and  $A_{SV}$  and the fits to the observations from the estimated model at a single location is shown in Figure S2 in Supporting Information S1.

Figure 2 shows azimuthal anisotropy from our model at depths of 20 and 60 km, and Figure S3 in Supporting Information S1 presents the corresponding uncertainty maps. At a depth of 20 km (Figure 2a), the azimuthal





**Figure 2.** Azimuthal anisotropy for the Juan de Fuca and Gorda plates at depths of (a) 20 km and (b) 60 km. The white bars indicate the fast orientations at each depth, with lengths proportional to amplitude. Background shows isotropic  $V_s$  variations at the corresponding depth from Wu et al. (2023). (c) Comparison of fast orientations from our model with those from  $P_n$  tomography (VanderBeek & Toomey, 2019). The white bars show the azimuthal anisotropy of our model, while the colored bars indicate  $P_n$  observations, colored by the angular differences from our results (see legend). The two blue arrows in the JdF MOR and JdF plate are plate-averaged  $P_n$  fast orientations compared with nearby fast orientations from our model, where the lengths are amplified. The means of the differences are indicated. (d) Similar to (c), but compared with SKS splitting (Bodmer et al., 2015).



**Figure 3.** Azimuthal anisotropy orientations with background amplitude of anisotropy at (a) 20 km and (e) 60 km. (b) Plate age from Wilson (1993) with the gradient-based quasi-paleo-spreading directions (QPS) (white bars). (c) Angular difference between azimuthal anisotropy fast orientations at 20 km depth and the quasi-paleo-spreading directions. White circled regions represent the regions inferred to be affected by propagator wakes and the Blanco Transform Fault. The black contour represents an angular difference of 15°. (d) Similar to (c), but with the augmented paleo-spreading model. (f) Two absolute plate motion models in the no-net-rotation reference frame. Red arrows represent MORVEL (DeMets et al., 2010), and blue arrows represent NUVEL1A (DeMets et al., 1994). The angular difference between azimuthal anisotropy fast orientations at 60 km with (g) MORVEL and (h) NUVEL1A. The average angular differences are indicated on each panel.

anisotropy reflects the tectonic history of the oceanic lithosphere. Near the present-day Juan de Fuca and Gorda spreading centers, the fast orientations are sub-normal to the strike of the mid-ocean ridge axes. In the Juan de Fuca plate, fast orientations turn to an EW orientation in the interior of the plate and to an NE-SW orientation near the northeast margin. In the interior of the Gorda plate, fast orientations show homogeneous NW-SE orientations. The fast orientations near the Blanco Transform Fault reflect a pattern similar to the interior of the JdF plate. The anisotropy at the northern end of JdF is stronger in amplitude than that in the interior of the JdF plate. Anisotropy measurements and isotropic observations have large uncertainty in the northern end of JdF and are probably influenced by the complex structure near the continental slope or by poor data quality (Zhang et al., 2021a).

At 60 km depth (Figure 2b), azimuthal anisotropy is expected to mainly reflect the features of the asthenosphere beneath the lithosphere, because the lithosphere is quite thin for this young oceanic plate. The amplitude of azimuthal anisotropy ( $A_{SV}$ ) is relatively small west of 127°W (Figure 3e) resulting in relatively large uncertainties in fast orientations (Figure S3b in Supporting Information S1). East of 127°W, the amplitude increases gradually,

and the fast orientations exhibit mainly sub-E-W orientations in the JdF plate and NE orientations in the Gorda plate, aligning sub-normally to the strike of the Cascadia trench.

The average uncertainties for the anisotropy fast orientations are  $9^\circ$  and  $15^\circ$  at depths of 20 and 60 km (Figure S3 in Supporting Information S1), respectively. The average uncertainty for amplitude is less than 0.4% (Figure S3 in Supporting Information S1) at these depths, while the eastern margin of the study region has a larger uncertainty due to the more limited azimuthal coverage there.

Azimuthal anisotropy in our deepest layer at 100 km is shown in Figure S4 in Supporting Information S1, but we refrain from detailed interpretation for the following reasons: First, the uncertainty of the observations of Rayleigh wave phase speed azimuthal anisotropy is large at the longest periods ( $>50$  s) as we have to rely on earthquake data alone (e.g., Figure S2a-b in Supporting Information S1; Eilon & Forsyth, 2020). The uncertainty for fast orientations is large in general, with a mean uncertainty of  $29^\circ$  (Figure S4b in Supporting Information S1). Second, vertical resolution for depths greater than 100 km is poor given the broader sensitivity kernels at long periods. Third, the estimated deep anisotropy amplitude is small (Figure S4a in Supporting Information S1). We also tested a two-layer-only inversion, and the fast orientation patterns of the upper two layers are similar to those in the three-layer model. We prefer to allow a third layer to absorb deeper sensitivity measurements, but will thus discuss only the top two layers.

## 4. Discussion

### 4.1. Comparison With *Pn* and *SKS*

*Pn* tomography provides constraints on the *P*-wave anisotropy at depths close to the base of the Moho. We compare our results in the lithosphere with a well-resolved *Pn* model in the Gorda plate (VanderBeek & Toomey, 2019) and plate-averaged fast orientations in the JdF plate (VanderBeek & Toomey, 2017), as shown in Figure 2c. The mean angular difference between *Pn* and our model in the Gorda plate is  $11^\circ$ , and the angular differences are  $8^\circ$  and  $10^\circ$  in the JdF interior and Endeavor ridges, respectively. Angular deviations are limited to the  $[0^\circ, 90^\circ]$  range, because we are comparing orientation with  $180^\circ$  periodicity. The consistency of fast orientations with small deviations between our results and the *Pn* model substantiates the reliability of our model in the lithosphere. The major sensitivity of our model to shallow structure comes from short-period ambient noise data ( $<20$  s), which help to constrain lithospheric structure compared to the surface wave inversion based on earthquake data which are typically restricted to longer periods. The *Pn* model contains stronger *P*-wave anisotropy ( $>5\%$ ) than our *S*-wave anisotropy estimate ( $<2\%$ ); this is expected from the larger relative *P*-wave anisotropy of olivine CPOs.

We also compare our inferred azimuthal anisotropy patterns in the asthenosphere with *SKS* splitting (Figure 2d). In general, the fast orientations of our model are consistent with *SKS* splitting. With an average angular difference of  $22^\circ$ , moderate deviations are found near the Blanco Transform Fault and the southern part of the Gorda plate. Because *SKS* measurements are a depth average, theoretically across the whole mantle, we do not expect an exact match of *SKS* with shallow surface wave anisotropy, as deeper anisotropy will affect measurements (e.g., Becker et al., 2012). In the shallow asthenosphere, the lack of smaller scale deviations between our results and *SKS* splits suggests a relatively simple mantle flow pattern beneath the JdF and northern Gorda plate. We attribute the observed smooth mismatch to the effects of layered anisotropy in the deeper asthenosphere (cf. Eilon & Forsyth, 2020). Beneath the southern Gorda plate, the deviation may reflect the influence of a deeper reorientation of mantle flow (e.g., Bodmer et al., 2015; Eilon & Forsyth, 2020; Martin-Short et al., 2015; Wang & Becker, 2019).

### 4.2. Fossil Azimuthal Anisotropy in the Oceanic Lithosphere

The dynamics of plate formation can be constrained from the paleo-spreading directions inferred from the gradient of seafloor age (e.g., Conrad & Lithgow-Bertelloni, 2007). Seismic azimuthal anisotropy measured in the oceanic lithosphere provides complementary constraints on the dynamics of plate formation. During seafloor spreading at mid-ocean ridges, peridotite mantle rock is pulled upward and then sheared; the olivine aggregates are thus affected by the transition from pure to simple shear during spreading (e.g., Blackman et al., 1996, 2017; Blackman & Kendall, 2002; Russell et al., 2022). The olivine CPO formed in rock retains the record of the local strain field and relative plate motion and is frozen in the oceanic lithosphere as it cools.

Global shear wave azimuthal anisotropy models provide large-scale anisotropy patterns based on earthquake data, with relatively low horizontal resolution and a lack of information about the lithosphere due to the typical period

range used (e.g., Becker & Lebedev, 2021; Beghein et al., 2014; Schaeffer et al., 2016). Local azimuthal anisotropy of the oceanic lithosphere is generally inferred using *Pn* tomography, which is limited by the local earthquake distribution and mainly provides information on the regions directly below the Moho. In contrast, ambient noise data from OBS arrays provide valuable shallow mantle information with depth resolution.

We estimate quasi-paleo-spreading directions by calculating the gradient of the magnetic anomaly inferred seafloor age (Wilson, 1993), with the results shown as white arrows in Figure 3b. Figure 3c shows the angular difference between the fast orientation of azimuthal anisotropy in the oceanic lithosphere and paleo-spreading orientations. In most of the JdFG system, the angular differences are smaller than 15°, as shown by the black contours in Figure 3c. Even in a young oceanic plate, such as the JdFG system, the fast orientations of seismic anisotropy thus already record the fossil spreading directions starting from the vicinity of the spreading center (cf. Becker et al., 2014; Debayle & Ricard, 2013). However, the tectonic-magmatic complexity of regional plate generation (Figure 1a) makes it difficult to infer the paleo-spreading from seafloor age gradients. In particular, the regions near three major propagator wakes (PW1-3 in Figure 3c) and the Blanco Transform Fault show large angular differences (>70°), where transform faults may be affected locally by the vertical mantle flow (Eakin et al., 2018). The propagator wake is formed through the propagation of a ridge segment across a small ridge offset into the preexisting oceanic crust formed by a receding ridge segment. As a result, the crust is transferred from one plate to another, and the plate age reserves along the spreading direction (Figure 1a; Hey et al., 1980). This process forms pseudo faults in isochron lines (Figure 1a) and complicates the quasi-paleo-spreading information from age gradients alone. In addition, near the immediate vicinity of the JdF spreading center, fast orientations mainly show a ridge-perpendicular pattern, while the derived quasi-paleo-spreading alignments are affected by local small-scale faults, leading to larger angular deviations (Figure 3c).

We thus also augmented the quasi-paleo-spreading model by replacing the spreading orientations in the regions of mid-ocean ridges, propagator wakes, and transform faults with the relative plate motion of the JdFG system relative to the Pacific plate based on the plate reconstruction of Wilson (1986, 1988), shown in Figure S5 in Supporting Information S1. Details about the updated quasi-paleo-spreading model are in Text S2 in Supporting Information S1. The seismic fast orientations indeed show an improved match with the paleo spreading orientations in the regions of mid-ocean ridges, propagator wakes, and the Blanco transform faults for this augmented model (Figure 3d). This indicates coherence of tectonic deformation between the surface as inferred from magnetic anomalies and at great depths where seismic imaging provides important complementary constraints for plate formation.

Besides the propagator wakes, there are also two regions with large angular differences near the trench, R1 and R2 in Figures 3c and 3d. The amplitude of anisotropy is quite small in R2 with a relatively large uncertainty in orientation. R1 corresponds to the area that has much younger seismic thermal ages than the plate age (Wu et al., 2023), probably reflecting the influence of deep fracturing structures due to subduction or ridge segment movement.

Compared to the relatively intact Juan de Fuca plate, the Gorda plate has experienced intense internal deformation (e.g., Chaytor et al., 2004) and the spreading rate decreases southward. Normal and strike-slip faults developed across the whole Gorda plate (Chaytor et al., 2004). The fast orientation of seismic anisotropy shows a homogeneous NW-SE pattern (Figure 3a), which does not reflect the influence of local faults with strike parallel to the ridge, possibly due to the lack of data in the shorter periods (<10 s). The isochrons near 42°N are offset by a small-scale propagator wake (Figure 1a). In most of the Gorda plate, fast orientations nevertheless align with quasi-paleo-spreading. Deviations between them appear to mainly reflect the influence of local strike-slip faults and propagator wakes on the plate age map.

### 4.3. Azimuthal Anisotropy in the Asthenosphere

For the asthenosphere beneath oceanic plates, the generally accepted cause of seismic anisotropy is CPO induced by mantle shear (e.g., Conrad & Behn, 2010; Tanimoto & Anderson, 1984). Absolute plate motion (APM) models are commonly used as a first-order estimate of the sense of shear caused by mantle flow and can often provide satisfactory approximations to more realistic CPO estimates based on solving for 3-D mantle circulation (Becker et al., 2014; Wang & Becker, 2019). Previous global studies show that APM models align well with orientations of azimuthal anisotropy in parts of the oceanic mantle (e.g., Becker et al., 2014; Debayle & Ricard, 2013).



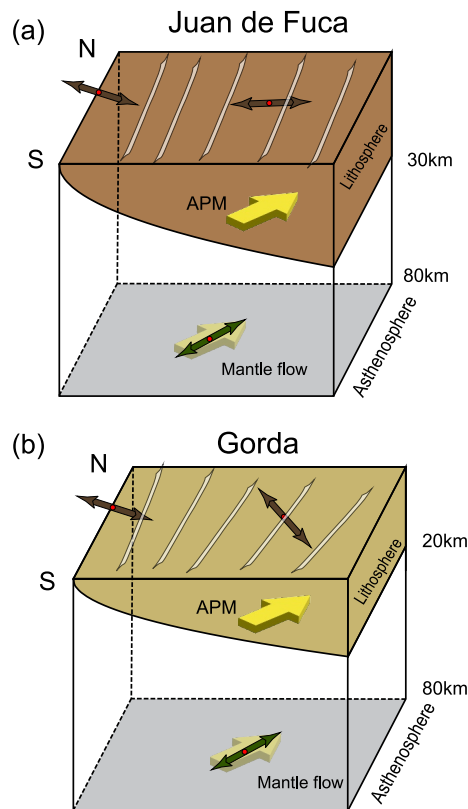


**Figure 4.** Interpretation of the azimuthal anisotropy pattern in the (a) Juan de Fuca and (b) Gorda plates. The top layer (oceanic lithosphere): the fast orientations of azimuthal anisotropy within the lithosphere are identified by the dark-brown (JdF) in (a) and light-brown (Gorda) arrows in (b), where the fast orientations reflect fossil anisotropy generated at the MOR and are parallel to the quasi-paleo-spreading directions. The stripes represent magnetic anomalies (cf. Figure 1a). Bottom layer (asthenosphere): The fast orientations in the asthenosphere are marked by dark-green arrows, where the fast orientations reflect anisotropy affected by the mantle flow and are parallel to the NUVEL1A APM model.

The comparison between our results and *SKS* elucidates the influence of deeper mantle flow. Beneath the JdF plate and the northern Gorda plate, the consistency between *SKS* and our results in the asthenosphere may indicate a single, consistent direction of mantle flow with depth, where shear is mainly aligned as inferred from NUVEL1A in the NNR APM frame. In contrast, beneath the southern Gorda plate (south of 42°N) and south of the Blanco Transform Fault, the moderate angular deviation between surface wave and *SKS* anisotropy reflects the effect of northwestward flow beneath the Pacific plate on the deeper asthenosphere (Eilon & Forsyth, 2020). Such variations are expected based on the local effects of density anomalies and the complexities of global mantle circulation (cf. Wang & Becker, 2019).

The amplitude of azimuthal anisotropy in the asthenosphere also shows systematic variations. Amplitude near the mid-ocean ridge in the Juan de Fuca and Gorda plates and Blanco Transform Fault is relatively small (<1%; cf. Eakin et al., 2018). The amplitude increases as the lithosphere moves away from the mid-ocean ridge, as expected for an actively forming asthenospheric anisotropy regime.

In summary, we image a relatively straightforward pattern of anisotropy where paleo-spreading dominates fossil at shallow depths and mantle flow actively forms anisotropy for deeper layers, respectively (Figure 4). This is noteworthy because the plate is relatively young and effects such as possible partial melt layers at depth (e.g., Hawley et al., 2016) might have been expected to complicate the seismo-tectonic setting. Besides confirming our general understanding of the formation and dynamics of the oceanic lithosphere-asthenosphere system, our

We first consider two APM models (Figure 3f) in a no-net rotation (NNR) reference frame, the MORVEL (DeMets et al., 2010) and NUVEL1A (DeMets et al., 1994) plate motion models. The angular differences between fast orientations of azimuthal anisotropy at 60 km depth and the APM models are shown in Figures 3g and 3h. Interestingly, the fast azimuthal anisotropy in the asthenosphere fits better with NUVEL1A than with MORVEL, with mean angular differences of 21° and 31° for NUVEL1A and MORVEL, respectively. In the interior of the Juan de Fuca and Gorda plates, the difference between seismic anisotropy fast orientation and the NUVEL1A model is smaller than 10° (Figure 3h), which indicates that the NUVEL1A model may reflect the mantle flow direction induced shear relevant during CPO formation at the imaged depths quite well. The angular deviation is relatively large near the margin of the study region (Figures 3g and 3h), probably due to the small amplitudes of anisotropy and hence large uncertainty for fast orientations as well as relatively poor azimuthal coverage.

We also investigate the impact of using different velocity reference frames. For plate motions relative to North America and the absolute spreading-aligned reference frame of Becker et al. (2015), which is close to hotspot reference frames, the mean angular differences are 25° and 27° for NUVEL1A and 34° and 52° for MORVEL in the comparison with seismic azimuthal anisotropy (Figure S6 in Supporting Information S1), respectively. This means that while the absolute angular mismatch depends on the choice of reference frame, the relative differences between NUVEL1A and MORVEL are robust.

One reason for the relatively poor match based on MORVEL may be that this model uses a relatively geologically recent, 0.78 Myr-averaging interval to determine the motion of the plate pair of the Juan de Fuca and Pacific, while NUVEL1A uses a 3.16 Myr-averaging interval (DeMets et al., 2010). In addition, plate motions determined with MORVEL agree better with GPS-based Euler pole estimates than NUVEL1A (DeMets et al., 2010). Therefore, while MORVEL more closely approximates current plate motions, NUVEL1A may reflect mantle flow directions in the asthenosphere, and hence tectonic fabrics in the incoming plate, on the timescales needed to form CPO anisotropy (cf. Becker, 2006).

analysis indicates that current convergence directions at the Cascadia margin may not reflect tectonic structures in the incoming plate and asthenosphere.

## 5. Conclusion

Based on a new Rayleigh wave phase velocity database, we construct a 3-D azimuthal anisotropy model of the lithosphere and asthenosphere in the Juan de Fuca and Gorda plates. In the lithosphere, the general fast orientation pattern of anisotropy within the interiors of the two plates aligns well with quasi-paleo-spreading from seafloor age gradients. Exceptions include regions influenced by transform faults and propagator wakes, where more detailed tectonic models improve the fit. In the asthenosphere, azimuthal anisotropy fast orientations that represent mantle flow fit well with plate motions inferred for ~3 Myr averaging periods rather than the more recent plate convergence. While anomalies such as due to melting or local buoyancy might be expected to be relatively more important for young plates, our findings show that young systems can record mantle convection in ways similar to older plates, such as the Pacific. Further exploration of higher-resolution anisotropy models, using both surface wave and body wave measurements as well as full-waveform inversion (FWI), can enhance our understanding of the details of plate formation, including recent plate reorganization and changes in plate boundary loading.

## Data Availability Statement

The surface wave dispersion dataset can be found in Zhang et al. (2021b). The azimuthal anisotropy model presented herein is available in Liu, Becker, et al. (2024). We used GMT by Wessel et al. (2019) for most of our figures.

## Acknowledgments

We thank the reviewers, Donald Forsyth and anonymous, for the constructive comments. We are grateful to Doug Wilson for providing constructive suggestions. We greatly appreciate the CI PI team and community members who contributed to the seismic data acquisition of Cascadia. Aspects of this research were supported by the NSF EAR 1537868 at the University of Colorado Boulder. C. Liu was supported by the JSG Distinguished Postdoctoral Fellowship at the University of Texas at Austin. TWB was partially funded by NSF EAR 192721, 2045292, and 2121666.

## References

- Becker, T. W. (2006). On the effect of temperature and strain-rate dependent viscosity on global mantle flow, net rotation, and plate-driving forces. *Geophysical Journal International*, 167(2), 943–957. <https://doi.org/10.1111/j.1365-246x.2006.03172.x>
- Becker, T. W., Conrad, C. P., Schaeffer, A. J., & Lebedev, S. (2014). Origin of azimuthal seismic anisotropy in oceanic plates and mantle. *Earth and Planetary Science Letters*, 401, 236–250. <https://doi.org/10.1016/j.epsl.2014.06.014>
- Becker, T. W., & Lebedev, S. (2021). Dynamics of the upper mantle in light of seismic anisotropy. *Geophysical Monograph Series*, 257–282. <https://doi.org/10.1002/9781119528609.ch10>
- Becker, T. W., Lebedev, S., & Long, M. D. (2012). On the relationship between azimuthal anisotropy from shear wave splitting and surface wave tomography: SKS splitting and tomography. *Journal of Geophysical Research*, 117(B1), n/a-n/a. <https://doi.org/10.1029/2011jb008705>
- Becker, T. W., Schaeffer, A. J., Lebedev, S., & Conrad, C. P. (2015). Toward a generalized plate motion reference frame. *Geophysical Research Letters*, 42(9), 3188–3196. <https://doi.org/10.1002/2015gl063695>
- Beghein, C., Yuan, K., Schmerr, N., & Xing, Z. (2014). Changes in seismic anisotropy shed light on the nature of the gutenber discontinuity. *Science*, 343(6176), 1237–1240. <https://doi.org/10.1126/science.1246724>
- Blackman, D. K., Boyce, D. E., Castelnaud, O., Dawson, P. R., & Laske, G. (2017). Effects of crystal preferred orientation on upper-mantle flow near plate boundaries: Rheologic feedbacks and seismic anisotropy. *Geophysical Journal International*, 210(3), 1481–1493. <https://doi.org/10.1093/gji/ggx251>
- Blackman, D. K., & Kendall, J.-M. (2002). Seismic anisotropy in the upper mantle 2. Predictions for current plate boundary flow models. *Geochemistry, Geophysics, Geosystems*, 3(9), 1–26. <https://doi.org/10.1029/2001gc000247>
- Blackman, D. K., Kendall, J.-M., Dawson, P. R., Wenk, H.-R., Boyce, D., & Morgan, J. P. (1996). Teleseismic imaging of subaxial flow at mid-ocean ridges: Traveltime effects of anisotropic mineral texture in the mantle. *Geophysical Journal International*, 127(2), 415–426. <https://doi.org/10.1111/j.1365-246x.1996.tb04730.x>
- Bodmer, M., Toomey, D. R., Hooft, E. E., Nábělek, J., & Braunmiller, J. (2015). Seismic anisotropy beneath the Juan de Fuca plate system: Evidence for heterogeneous mantle flow. *Geology*, 43(12), 1095–1098. <https://doi.org/10.1130/g37181.1>
- Chaytor, J. D., Goldfinger, C., Dziak, R. P., & Fox, C. G. (2004). Active deformation of the Gorda plate: Constraining deformation models with new geophysical data. *Geology*, 32(4), 353–356. <https://doi.org/10.1130/g20178.2>
- Conrad, C. P., & Behn, M. D. (2010). Constraints on lithosphere net rotation and asthenospheric viscosity from global mantle flow models and seismic anisotropy. *Geochemistry, Geophysics, Geosystems*, 11(5). <https://doi.org/10.1029/2009gc002970>
- Conrad, C. P., & Lithgow-Bertelloni, C. (2007). Faster seafloor spreading and lithosphere production during the mid-Cenozoic. *Geology*, 35(1), 29–32. <https://doi.org/10.1130/g22759a.1>
- Debayle, E., & Ricard, Y. (2013). Seismic observations of large-scale deformation at the bottom of fast-moving plates. *Earth and Planetary Science Letters*, 376, 165–177. <https://doi.org/10.1016/j.epsl.2013.06.025>
- DeMets, C., Gordon, R. G., & Argus, D. F. (2010). Geologically current plate motions. *Geophysical Journal International*, 181(1), 1–80. <https://doi.org/10.1111/j.1365-246x.2009.04491.x>
- DeMets, C., Gordon, R. G., Argus, D. F., & Stein, S. (1994). Effect of recent revisions to the geomagnetic reversal time scale on estimates of current plate motions. *Geophysical Research Letters*, 21(20), 2191–2194. <https://doi.org/10.1029/94gl02118>
- Eakin, C. M., Rychert, C. A., & Harmon, N. (2018). The role of oceanic transform faults in seafloor spreading: A global perspective from seismic anisotropy. *Journal of Geophysical Research: Solid Earth*, 123(2), 1736–1751. <https://doi.org/10.1002/2017jb015176>
- Eilon, Z. C., & Forsyth, D. W. (2020). Depth-Dependent Azimuthal Anisotropy Beneath the Juan de Fuca Plate System. *Journal of Geophysical Research: Solid Earth*, 125(8). <https://doi.org/10.1029/2020jb019477>

- Feng, L., Liu, C., & Ritzwoller, M. H. (2020). Azimuthal anisotropy of the crust and uppermost mantle beneath Alaska. *Journal of Geophysical Research: Solid Earth*, 125(12), e2020JB020076. <https://doi.org/10.1029/2020jb020076>
- Francis, T. (1969). Generation of seismic anisotropy in the upper mantle along the mid-oceanic ridges. *Nature*, 221(5176), 162–165. <https://doi.org/10.1038/221162b0>
- Hawley, W. B., Allen, R. M., & Richards, M. A. (2016). Tomography reveals buoyant asthenosphere accumulating beneath the Juan de Fuca plate. *Science*, 353(6306), 1406–1408. <https://doi.org/10.1126/science.aad8104>
- Hey, R., Duennebie, F. K., & Morgan, W. J. (1980). Propagating rifts on midocean ridges. *Journal of Geophysical Research*, 85(B7), 3647–3658. <https://doi.org/10.1029/jb085ib07p03647>
- Karato, S., Jung, H., Katayama, I., & Skemer, P. (2008). Geodynamic significance of seismic anisotropy of the upper mantle: New insights from laboratory studies. *Annual Review of Earth and Planetary Sciences*, 36(1), 59–95. <https://doi.org/10.1146/annurev.earth.36.031207.124120>
- Lin, F., & Ritzwoller, M. H. (2011). Apparent anisotropy in inhomogeneous isotropic media. *Geophysical Journal International*, 186(3), 1205–1219. <https://doi.org/10.1111/j.1365-246x.2011.05100.x>
- Lin, F., Ritzwoller, M. H., Yang, Y., Moschetti, M. P., & Fouch, M. J. (2011). Complex and variable crustal and uppermost mantle seismic anisotropy in the western United States. *Nature Geoscience*, 4(1), 55–61. <https://doi.org/10.1038/ngeo1036>
- Liu, C., Becker, T. W., Wu, M., Han, S., & Ritzwoller, M. H. (2024). Seismic Azimuthal Anisotropy Within and Beneath the Juan de Fuca-Gorda Plate System (v1.0). *Zenodo*. [Dataset]. <https://doi.org/10.5281/zenodo.14031389>
- Liu, C., & Ritzwoller, M. H. (2024). Seismic anisotropy and deep crustal deformation across Alaska. *Journal of Geophysical Research: Solid Earth*, 129(5), e2023JB028525. <https://doi.org/10.1029/2023jb028525>
- Liu, C., Sheehan, A. F., & Ritzwoller, M. H. (2024). Seismic azimuthal anisotropy beneath the Alaska subduction zone. *Geophysical Research Letters*, 51(14), e2024GL109758. <https://doi.org/10.1029/2024GL109758>
- Liu, C., Yao, H., Yang, H., Shen, W., Fang, H., Hu, S., & Qiao, L. (2019). Direct inversion for three-dimensional shear wave speed azimuthal anisotropy based on surface wave ray tracing: Methodology and application to yunnan, southwest China. *Journal of Geophysical Research: Solid Earth*, 124(11), 11394–11413. <https://doi.org/10.1029/2018jb016920>
- Liu, C., Zhang, S., Sheehan, A. F., & Ritzwoller, M. H. (2022). Surface wave isotropic and azimuthally anisotropic dispersion across Alaska and the Alaska-Aleutian subduction zone. *Journal of Geophysical Research: Solid Earth*, 127(11). <https://doi.org/10.1029/2022jb024885>
- Long, M. D., & Becker, T. W. (2010). Mantle dynamics and seismic anisotropy. *Earth and Planetary Science Letters*, 297(3–4), 341–354. <https://doi.org/10.1016/j.epsl.2010.06.036>
- Martin-Short, R., Allen, R. M., Bastow, I. D., Totten, E., & Richards, M. A. (2015). Mantle flow geometry from ridge to trench beneath the Gorda-Juan de Fuca plate system. *Nature Geoscience*, 8(12), 965–968. <https://doi.org/10.1038/ngeo2569>
- Montagner, J.-P., Griot-Pommer, D., & Lavé, J. (2000). How to relate body wave and surface wave anisotropy? *Journal of Geophysical Research*, 105(B8), 19015–19027. <https://doi.org/10.1029/2000jb900015>
- Montagner, J. P., & Nataf, H. C. (1986). A simple method for inverting the azimuthal anisotropy of surface waves. *Journal of Geophysical Research*, 91(B1), 511–520. <https://doi.org/10.1029/JB091iB01p00511>
- Nedimović, M. R., Bohnenstiehl, D. R., Carbotte, S. M., Canales, J. P., & Dziak, R. P. (2009). Faulting and hydration of the Juan de Fuca plate system. *Earth and Planetary Science Letters*, 284(1–2), 94–102. <https://doi.org/10.1016/j.epsl.2009.04.013>
- Nicolas, A., & Christensen, N. I. (1987). Composition, structure and dynamics of the lithosphere-asthenosphere system. *Geodynamics Series*, 111–123. <https://doi.org/10.1029/gd016p0111>
- Nishimura, C. E., & Forsyth, D. W. (1989). The anisotropic structure of the upper mantle in the Pacific. *Geophysical Journal International*, 96(2), 203–229. <https://doi.org/10.1111/j.1365-246x.1989.tb04446.x>
- Ren, X., Liu, X., & Zhao, D. (2024). Subduction transforms azimuthal anisotropy in the Juan de Fuca plate. *Tectonophysics*, 877, 230272. <https://doi.org/10.1016/j.tecto.2024.230272>
- Riddiough, R. P. (1984). Recent movements of the Juan de Fuca plate system. *Journal of Geophysical Research*, 89(B8), 6980–6994. <https://doi.org/10.1029/JB089iB08p06980>
- Ritzwoller, M. H., Shapiro, N. M., & Zhong, S.-J. (2004). Cooling history of the Pacific lithosphere. *Earth and Planetary Science Letters*, 226(1–2), 69–84. <https://doi.org/10.1016/j.epsl.2004.07.032>
- Russell, J. B., Gaherty, J. B., Mark, H. F., Hirth, G., Hansen, L. N., Lizarralde, D., et al. (2022). Seismological evidence for girdled olivine lattice-preferred orientation in oceanic lithosphere and implications for mantle deformation processes during seafloor spreading. *Geochemistry, Geophysics, Geosystems*, 23(10). <https://doi.org/10.1029/2022gc010542>
- Schaeffer, A. J., Lebedev, S., & Becker, T. W. (2016). Azimuthal seismic anisotropy in the Earth's upper mantle and the thickness of tectonic plates. *Geophysical Journal International*, 207(2), 901–933. <https://doi.org/10.1093/gji/ggw309>
- Smith, D. B., Ritzwoller, M. H., & Shapiro, N. M. (2004). Stratification of anisotropy in the Pacific upper mantle. *Journal of Geophysical Research*, 109(B11). <https://doi.org/10.1029/2004jb003200>
- Smith, M. L., & Dahlen, F. A. (1973). The azimuthal dependence of love and Rayleigh wave propagation in a slightly anisotropic medium. *Journal of Geophysical Research*, 78(17), 3321–3333. <https://doi.org/10.1029/JB078i017p03321>
- Tanimoto, T., & Anderson, D. L. (1984). Mapping convection in the mantle. *Geophysical Research Letters*, 11(4), 287–290. <https://doi.org/10.1029/gl011i004p00287>
- Toomey, D., Allen, R., Barclay, A., Bell, S., Bromirski, P., Carlson, R., et al. (2014). The Cascadia initiative: A sea change in seismological studies of subduction zones. *Oceanography*, 27(2), 138–150. <https://doi.org/10.5670/oceanog.2014.49>
- VanderBeek, B. P., & Toomey, D. R. (2017). Shallow mantle anisotropy beneath the Juan de Fuca plate. *Geophysical Research Letters*, 44(22), 11382–11389. <https://doi.org/10.1002/2017GL074769>
- VanderBeek, B. P., & Toomey, D. R. (2019). Pn Tomography of the Juan de Fuca and Gorda Plates: Implications for Mantle Deformation and Hydration in the Oceanic Lithosphere. *Journal of Geophysical Research: Solid Earth*, 124(8), 8565–8583. <https://doi.org/10.1029/2019jb017707>
- Wang, W., & Becker, T. W. (2019). Upper mantle seismic anisotropy as a constraint for mantle flow and continental dynamics of the North American plate. *Earth and Planetary Science Letters*, 514, 143–155. <https://doi.org/10.1016/j.epsl.2019.03.019>
- Wessel, P., Luis, J. F., Uieda, L., Scharroo, R., Wobbe, F., Smith, W. H. F., & Tian, D. (2019). The generic mapping tools version 6. *Geochemistry, Geophysics, Geosystems*, 20(11), 5556–5564. <https://doi.org/10.1029/2019gc008515>
- Wilson, D. S. (1986). A kinematic model for the Gorda Deformation Zone as a diffuse southern boundary of the Juan de Fuca Plate. *Journal of Geophysical Research*, 91(B10), 10259–10269. <https://doi.org/10.1029/jb>
- Wilson, D. S. (1988). Tectonic history of the Juan de Fuca Ridge over the last 40 million years. *Journal of Geophysical Research*, 93(B10), 11863–11876. <https://doi.org/10.1029/jb093ib10p11863>

- Wilson, D. S. (1993). Confidence intervals for motion and deformation of the Juan de Fuca Plate. *Journal of Geophysical Research*, 98(B9), 16053–16071. <https://doi.org/10.1029/93jb01227>
- Wu, M., & Ritzwoller, M. H. (2023). Asymmetric seafloor depth across the Juan de Fuca Ridge caused by lithospheric heating. *Communications Earth & Environment*, 4(1), 408. <https://doi.org/10.1038/s43247-023-01072-1>
- Wu, M., Wang, H., Zhang, S., & Ritzwoller, M. H. (2023). Plate Age and Uppermost Mantle Structure Across the Juan de Fuca and Gorda Plates. *Journal of Geophysical Research: Solid Earth*, 128(8). <https://doi.org/10.1029/2023jb026494>
- Zhang, S., Wang, H., Wu, M., & Ritzwoller, M. H. (2021a). Isotropic and azimuthally anisotropic Rayleigh wave dispersion across the Juan de Fuca and Gorda plates and U.S. Cascadia from earthquake data and ambient noise two- and three-station interferometry. *Geophysical Journal International*, 226(2), 862–883. <https://doi.org/10.1093/gji/ggab142>
- Zhang, S., Wang, H., Wu, M., & Ritzwoller, M. H. (2021b). Isotropic and azimuthally anisotropic Rayleigh wave dispersion maps across Cascadia (v2). *Zenodo*. [Dataset]. <https://doi.org/10.5281/zenodo.4792450>